Probing the elastic coupling at van der Waals interfaces of two-dimensional materials

Xiaomeng Wang,[1,*] Erteng Chen,[2,*] Qianglong Wu,[1,*] Xiaoyi Yuan,[1,3] Tianyi Zhang,[1] Shuze Zhu,[1,3,†] Zhaohe Dai,[2,‡] and Yang Gao[1,3,∥]

[1]*Center for X-Mechanics, Department of Engineering Mechanics, Zhejiang University, Hangzhou 310027, China*
[2]*Department of Mechanics and Engineering Science, College of Engineering, Peking University, Beijing 100871, China*
[3]*Key Laboratory of Soft Machines and Smart Devices of Zhejiang Province, Zhejiang University, Hangzhou 310027, China*

(Received 23 October 2024; accepted 10 March 2025; published 25 March 2025)

The van der Waals interfaces play a crucial role in determining the physical properties and enhancing the device performances of two-dimensional materials. Here we report the investigation of the elastic coupling at the van der Waals interfaces between graphene layers and silicon oxide, via angstrom-indentation experiments combined with density functional theoretical calculations. By developing a theoretical model based on the Lennard-Jones potential, we demonstrate that the effective elastic modulus of the graphene/silicon oxide van der Waals interface is approximately 1.6 GPa, and the interlayer elastic modulus for graphene is 34.2 GPa. In addition, contact stiffness mapping of graphene with various numbers of layers on a silicon oxide substrate indicates that the very first two-dimensional (2D) layer could significantly screen the 2D–three-dimensional interface interactions.

DOI: 10.1103/PhysRevB.111.125418

I. INTRODUCTION

Two-dimensional (2D) materials have attracted a large amount of attention in the past two decades, owing to their exceptional physical properties and application prospects [1–4]. In most of their applications (next-generation electronics, energy storage, sensors, etc.), 2D materials are fabricated on certain three-dimensional (3D) bulk substrates [5–8]. The 2D-3D interfacial interactions, mostly arising from the van der Waals (vdW) coupling, could substantially influence the physical, chemical, and mechanical properties of the supported 2D materials [9–13], subsequently impacting the performance of the 2D electronic devices [14–16]. Moreover, novel physics and new applications have been intensively reported in the vertical stacking of various 2D materials via the 2D-2D interfacial vdW interactions [17–24]. Therefore, to fully exploit the promising applications of 2D materials and their heterostructures, it is of great significance to accurately probe and modulate the vdW interactions at the interfaces of 2D materials, where the interfacial physics, chemistry, and mechanics are closely intertwined [9,25]. Among the extensive theoretical and experimental approaches on the complex interfacial mechanics of 2D materials, characterization of the elastic response by measuring the force-deformation relationship is a convenient and effective methodology.

Nanoindentation based on atomic force microscopy (AFM) has been proven powerful in mechanically characterizing the intralayer and interlayer couplings in 2D materials [26–30]. However, investigation of the elastic coupling at the 2D material vdW interfaces, especially the 2D-3D interface, remains an experimental challenge because it requires extremely shallow indentation, less than the interfacial distance, that is, usually a few angstroms. We previously reported a modulated nanoindentation method, also termed angstrom indentation, which allows for angstrom-scale indentation depth and subangstrom vertical resolution [31]. The enhanced resolution of angstrom indentation has enabled the direct measurement of the interlayer elasticity of few-layer graphene and graphene oxide films [27] and has led to the discovery of the room-temperature diamondization of epitaxial bilayer graphene on silicon carbide [32–34]. Another critical challenge for the indentation measurements for the 2D-3D interface is that the classical contact mechanics theories are not applicable, due to the high anisotropy of 2D materials and the adhesive interaction between the indenter and the testing material.

In this work, we thoroughly investigate the elastic coupling at the vdW interface between graphene and silicon oxide substrate—the most typical 2D material and substrate, using angstrom indentation combined with a theoretical model and density functional theoretical (DFT) calculations. On the foundation of the qualitative experimental result, we developed a unique theoretical contact model to quantify the elastic coupling at the 2D-3D vdW interface of graphene and silicon oxide, as well as the interlayer coupling between graphene layers. The obtained interlayer elastic modulus of graphene is 34.2 GPa, which coincides with the previously reported values extremely well [27,35], confirming the validity of our experiments and theoretical model. More importantly, the effective Young's modulus for the vdW interface between graphene and silicon oxide is achieved, which is ∼1.6 GPa. Furthermore, we mapped the out-of-plane stiffness of the mono- and bilayer graphene as well as the silicon oxide substrate through

*These authors contributed equally to this work.
†Contact author: shuzezhu@zju.edu.cn
‡Contact author: daizh@pku.edu.cn
∥Contact author: ygao96@zju.edu.cn

 ©2025 American Physical Society

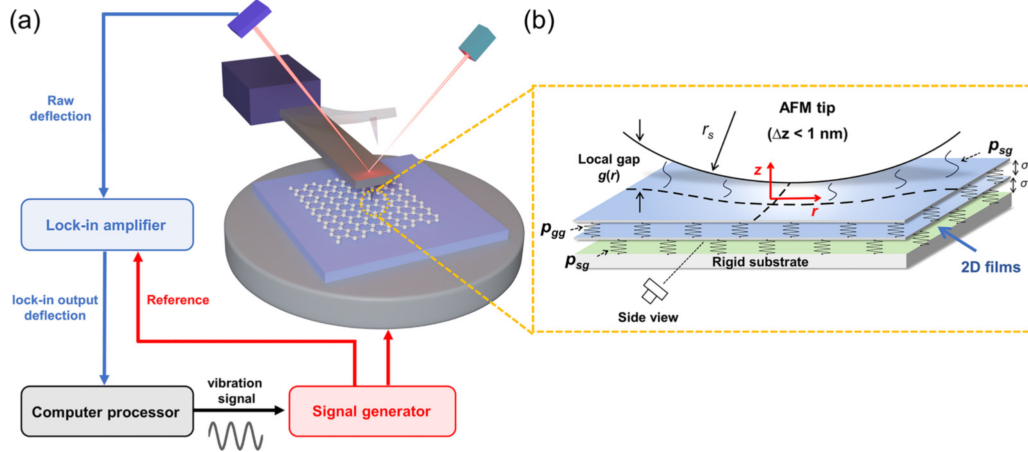

FIG. 1. (a) Schematic of the angstrom-indentation experimental setup via contact-resonance AFM. (b) Schematic illustration of the theoretical model for angstrom indentation on few-layer 2D materials placed on a rigid substrate. The 2D films are bonded by vertical nonlinear van der Waals force springs. The side view with more details is displayed in Fig. 3.

contact-resonance (CR) AFM. Consistent with our DFT calculations, the monolayer graphene region is significantly less stiff than the substrate in a wide range of normal forces, while the effective out-of-plane stiffness for the bilayer region is smaller but quite close to the monolayer region, indicating that the impact from the substrate can be significantly screened by the first 2D layer.

II. ANGSTROM INDENTATION VIA CONTACT-RESONANCE AFM

Angstrom indentation can quantitatively characterize the interlayer mechanics of 2D materials perpendicular to the layers at pressures of a few tens of nano-Newtons. Previous work has reported that when the 2D film is thicker than 10 layers, the influence of the rigid substrate on the out-of-plane mechanical properties for the 2D film is negligible [27], meaning the effective out-of-plane elastic modulus is simply the interlayer elastic modulus of the 2D material. When the 2D film thickness is down to below 5 layers, the substrate effect has to be taken into consideration. The interfacial distance between 2D materials and the substrate underneath is usually on the order of 0.1 nm. Therefore, in order to mechanically quantify the vdW interactions between 2D materials and the substrate, the indentation depth has to be on the same order as the interfacial distance, ensuring that the effect of the substrate deformation can be neglected.

Contact-resonance AFM is realized by inputting a vertical excitation signal to either the cantilever or the sample; the resonance frequency and quality factor of the cantilever change according to the viscoelastic properties of the sample. The resonance amplitude of the tip-to-sample distance can be reduced to the picometer level, allowing for extremely high sensitivity and vertical resolution while indenting only a few angstroms. Therefore, CRAFM can be directly adopted to perform angstrom indentation to characterize the elastic coupling at the interface of 2D materials and the substrate [36–38]. The experimental setup for angstrom indentation based on CRAFM is displayed in Fig. 1(a). The AFM cantilever is oscillated by the piezoelectric actuator, while the tip is in contact with the sample surface under a certain normal force. The excitation signal of the piezoelectric actuator is from a function generator that sends a continuous sine wave signal with adjustable frequency and amplitude. The variation of the vibration amplitude and frequency of the cantilever are recorded by a lock-in amplifier through the AFM photodiode detector as the feedback control signal. Furthermore, the sync signal from the function generator provides the reference signal for the lock-in amplifier. In this way, the spectrum of the vibration amplitude versus frequency is recorded. The resonance frequency of the cantilever, when the tip is in contact with the sample, is related to the effective contact stiffness k_{contact}, based on the Euler-Bernoulli beam theory. The tip-sample contact stiffness k_{contact} strongly depends on the out-of-plane deformation and the tip-sample vdW interactions, especially with angstrom-scale deformation as shown in Fig. 1(b). See more details on the experimental setup and background theory in the Supplemental Material [39] (also see Refs. [40–48]). The angstrom-indentation experiments via CRAFM are performed in tip-retraction mode to eliminate the "snap-in" effect in the tip-approaching process, due to the existence of the long-range adhesive forces between the tip and sample. More specifically, during the angstrom-indentation measurement, the tip is approached on the sample surface with a preset normal load (e.g., 50 nN) to ensure the tip and sample are in contact; then the normal load applied to the tip is progressively reduced until the contact with the surface is lost.

III. SINGLE-POINT ANGSTROM-INDENTATION EXPERIMENTS

We first examine the elastic coupling between the substrate and the very first layer of the supported graphene films via angstrom indentation. Graphene flakes were mechanically exfoliated onto silicon wafers with a ∼285 nm oxidation layer. Figure 2(a) illustrates the AFM topographic image of a monolayer graphene on silicon oxide. Angstrom indentation based on CRAFM was then performed on the monolayer graphene in Fig. 2(a) as well as the bare substrate nearby as a reference.

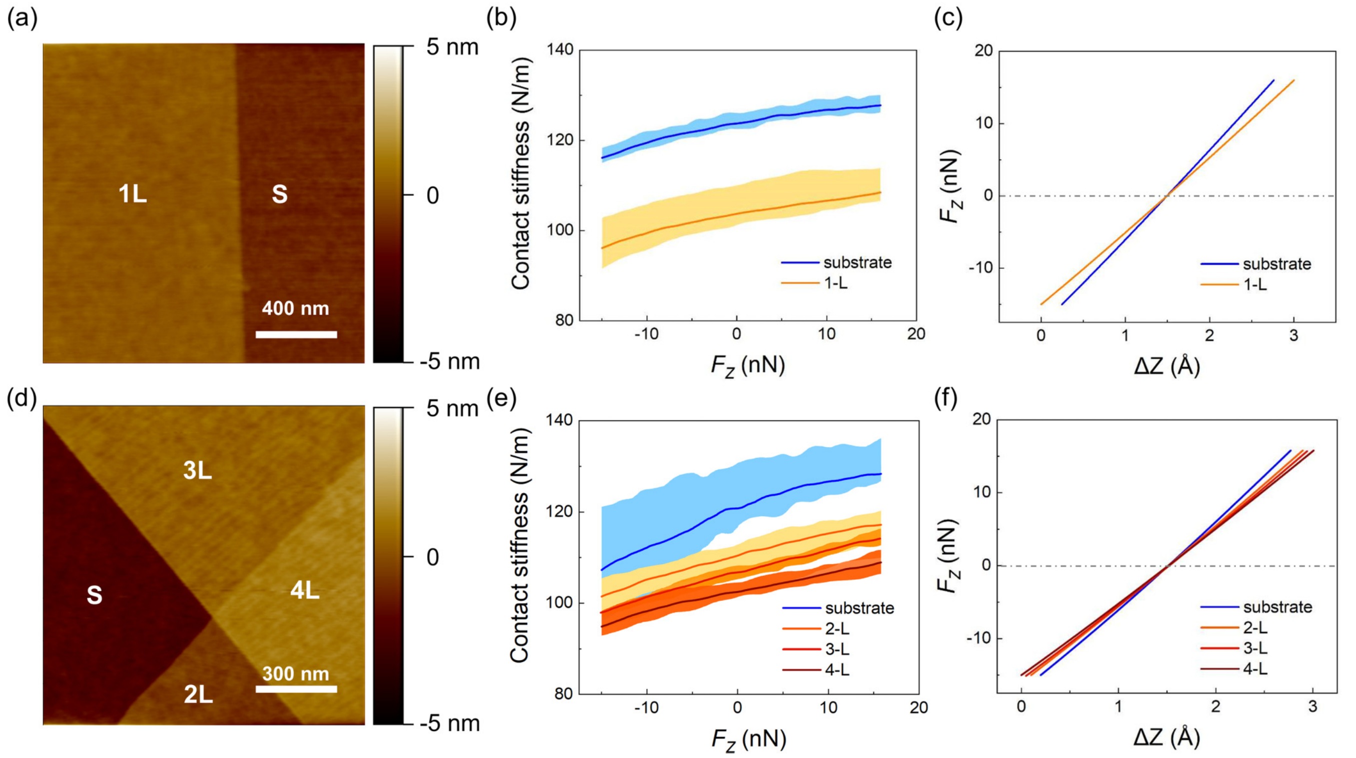

FIG. 2. (a) AFM topographic image of monolayer graphene on silicon oxide. (b) Contact stiffnesses of monolayer graphene and the silicon oxide substrate as a function of the loading force. The light-colored regions and deep-colored lines represent the data ranges and the corresponding averaged curves, respectively. (c) Indentation curves for the monolayer graphene and the silicon oxide substrate. (d) AFM topographic image of a region with substrate, two-, three-, and four-layer graphene. The light-colored regions and deep-colored lines represent the data ranges and the corresponding averaged curves, respectively. (e) Contact stiffnesses of the graphene with different thicknesses and the silicon oxide under various loading forces. (f) Indentation curves for the graphene with different thicknesses and the silicon oxide substrate.

The contact stiffness k_{contact} of the monolayer graphene and the silicon substrate, as a function of the normal force F_Z, are plotted in Fig. 2(b). The raw data of the indentation experiment are presented in Fig. S3 in the Supplemental Material [39]. Multiple measurements were randomly performed on the graphene and substrate; the variations of all the obtained curves are marked by the light-colored regions and the averaged curves are represented by the deep-colored lines in Fig. 2(b). Obviously, the contact stiffness k_{contact} of silicon oxide is always greater than the case in which a monolayer graphene is placed on top. Specifically, as the loading force decreases from 15 to -15 nN, the k_{contact} of the silicon oxide substrate decreases from 125 to 115 N/m, while k_{contact} of the monolayer graphene decreases from 106 to 96 N/m. As mentioned in Sec. II, the angstrom indentation is performed in the tip-retraction process, so the "negative" normal force in Fig. 2 indicates the attractive adhesive force between the tip and sample surface. Note that the contact stiffness k_{contact} is simply the slope of the force-indentation curve. Therefore, once we collect the k_{contact} for each normal force F_N, we can simply use Eq. (1) to perform an integral and obtain the force-indentation curve. This "indirect measurement and integration" strategy could significantly enhance the vertical resolution and greatly eliminate the influence of thermal noise.

$$\triangle Z(F_N) = \int \frac{dF_N}{k_{\mathrm{contact}}(F_N)}. \quad (1)$$

Figure 2(c) demonstrates the loading force versus indentation curves derived from Fig. 2(b). The indentation depth varies by about 3 Å, which is close to the thickness of a monolayer graphene, i.e., the interfacial distance between monolayer graphene and substrate. In the classical Hertzian or Derjaguin-Muller-Toporov (DMT) contact models, the "zero-deformation" point corresponds to the "zero-contact area" point where the tip and sample seperate. In practical measurements, it is extremely difficult to capture the exact "zero-contact" point, since the AFM tip usually detaches before the contact area decreases to zero, due to factors such as surface roughness of the tip or surface defects on the sample. In the Johnson-Kendall-Roberts (JKR) model, the relationship between the contact area and deformation is more complicated, making the definition of a "zero-contact" point more challenging. More importantly, classical models are technically valid only for isotropic solids, while 2D materials are highly anisotropic, especially when there are only one or two layers. On the other hand, the "zero-force" point, which corresponds to the statically equilibrium state of the tip-2D-3D system and is independent of contact models, can be accurately and easily determined by the deflection signal of the AFM cantilever. Moreover, the contact stiffness of the zero-force point gives important information of the nonlinear vdW interacting phenomena at the 2D-2D and 2D-3D interfaces. Therefore, the "zero-force" point is not only easier to identify, but also more physically significant than

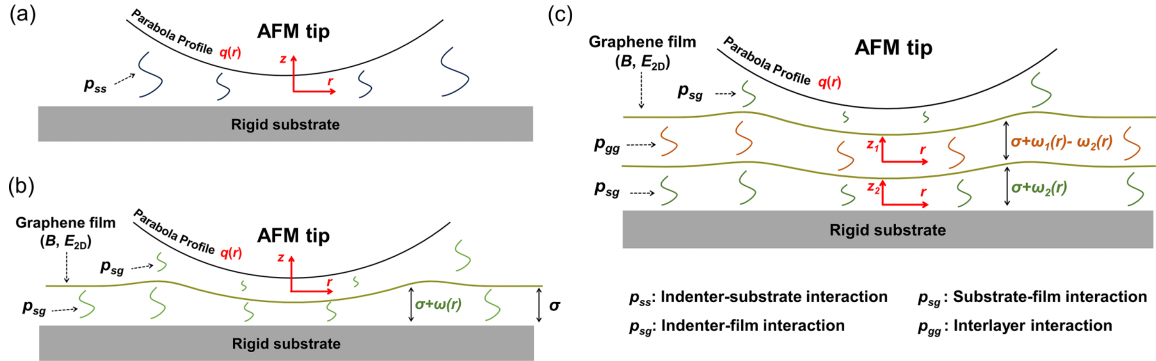

FIG. 3. (a)–(c) Schematic illustration of theoretical indentation model, i.e., the "side view" in Fig. 1. Here, graphene films with bending stiffness B and in-plane modulus E_{2D} are bonded by vertical nonlinear vdW springs (described by P_{sg} and P_{gg}). Given that the indenter radius r_s is much larger than the equilibrium distance σ, the spherical indenter can be approximately modeled as a parabola $q(r) = s + r^2/2r_s$, where s is the vertical separation between the bottom of the indenter and the equilibrium position of the uppermost graphene film [50,51].

the "zero-deformation" point. Therefore, we offset the indentation curves horizontally such that they all intersect at the $F_Z = 0$ point, for a more straightforward comparison.

Figure 2(d) illustrates the AFM topographic image of another graphene flake on silicon oxide, where the number of graphene layers is marked. The number of layers was identified through Raman spectroscopy and height profile in the AFM topographic image. The variations of all the obtained contact stiffnesses are marked by the light color and the corresponding averaged curves are represented by the deep-colored lines in Fig. 2(e). The corresponding indentation curves derived via Eq. (1) are plotted in Fig. 2(f). See Fig. S4 in the Supplemental Material for the raw data [39]. The contact stiffness k_{contact} of the silicon oxide substrate decreases from 130 to 106 N/m, and those for two-, three-, and four-layer graphene decrease from 117 to 102 N/m, 112 to 98 N/m, and 108 to 95 N/m, respectively. The contact stiffnesses for two-, three-, and four-layer graphene are very close, indicating that the interlayer elastic coupling of graphene is much stronger than the interfacial elastic coupling between graphene and silicon oxide. Furthermore, with an increase in the number of graphene layers, the divergence in contact stiffness between graphene and substrate augments, suggesting that the impact of the underlying silicon oxide substrate on the out-of-plane elastic properties of graphene gradually diminishes as the number of layers increases.

IV. THEORETICAL MODELING

As shown in Fig. 2, the measured force-indentation curves all exhibit a nearly linear behavior near the zero-force point. The slope of those force-indentation curves at the zero-force point, which we define as "indentation stiffness," could provide us valuable quantitative insights into the intrinsic vertical elastic properties of the vdW interfaces within 2D layers or between the 2D layer and the substrate/indenter interface. However, this problem is complicated by the interplay between the in-plane elasticity of the 2D sheet, the interlayer vdW interaction in 2D layers, and the adhesive interaction between the tip and the testing material. As a result, classical contact mechanics models such as Hertzian, DMT, and JKR do not apply to our problem [49].

We begin with a simple scenario: angstrom indentation on bare substrate as shown in Fig. 3(a). To characterize the indenter/substrate interface, we employ the classical additive Lennard-Jones potential [49], giving the interfacial traction-separation relation as

$$p_{\text{ss}}(g) = \frac{E_{\text{ss}}}{6}\left[\left(\frac{\sigma}{g(r)}\right)^3 - \left(\frac{\sigma}{g(r)}\right)^9\right]. \tag{2}$$

Here the subscript "ss" represents "solid-solid" interactions per unit area. We note that in the calculation of local van der Waals forces, the indenter and the substrate are considered as two infinite half-spaces of the same material (referred to here as "solid"), $g(r)$ is the local gap of the indenter/substrate interface (as illustrated in Fig. 1), and σ is the local equilibrium spacing where the interfacial traction is zero [$p_{\text{ss}}(\sigma) = 0$]. E_{ss} is the linearized stiffness of the vdW interface under transverse loading, evaluated near the zero-indentation spacing, i.e., $\frac{E_{\text{ss}}}{\sigma} = \frac{dp_{\text{ss}}}{dg}|_{g=\sigma}$. We note that the equilibrium spacing σ is defined for two flat surfaces. In experiments using a spherical indenter of radius r_s, letting $g(0) = \sigma$ does not lead to the zero-indentation force. Instead, zero-indentation force occurs when tip-substrate gap $g(0)$ is slightly below local equilibrium spacing σ, specifically $\sigma/4^{1/6}$. At this position, a small region near the spherical tip experiences repulsive interfacial interactions, while the rest of the interface experiences attractive interactions so that an overall equilibrium is established. By perturbing the sphere around this equilibrium point, we can determine the indentation stiffness of the indenter/substrate interface (see more details in Appendix A):

$$K_0 = 2\pi E_{\text{ss}} r_s. \tag{3}$$

Here the subscript "0" presents the number of graphene layers existing between the tip and the substrate. Using our measurements on bare substrates and applying them to Eq. (3), we find E_{ss} to be ~0.69 GPa.

We then proceed to angstrom indentation on the substrate-supported monolayer graphene, as shown in Fig. 3(b). The presence of the graphene layer between the indenter and the substrate results in the formation of two graphene/substrate

vdW interfaces (as both the indenter and the substrate are made of silicon oxide). In this context, the interfacial traction-separation relation follows the form of the vdW interaction between a half-space and a thin layer:

$$p_{sg}(g) = \frac{E_{sg}}{6}\left[\left(\frac{\sigma}{g(r)}\right)^4 - \left(\frac{\sigma}{g(r)}\right)^{10}\right]. \quad (4)$$

Here the subscript "sg" represents "solid-graphene" interactions, and E_{sg} is the linearized stiffness of the graphene/substrate interface. Evidently, compared to Eq. (2), the finite thickness of the film results in a different power-law relationship. Unlike the indentation of bare substrate discussed previously, the bending and stretching of the graphene sheet introduce significant challenges in determining the gap between the indenter tip and graphene film at zero-force point. However, at small indentation depth, the elastic properties of the film have limited effect (see discussion in Appendix B and justification in the Supplemental Material [39]), allowing us to anticipate an expression similar to Eq. (3) for the indentation stiffness K_1:

$$K_1 = \alpha_1 E_{sg} r_s + \beta_1, \quad (5)$$

where $\alpha_1 = 2.4958$, $\beta_1 = -1.1666$ are numerically determined constants. To perform such fitting, we inevitably fix E_{sg} while fitting the $K_1 \sim r_s$ curve. It remains unclear whether this fixed E_{sg} value will affect the final results, so we adopt an iterative fitting method to address such complexity (also shown in the flow chart in Fig. S8 [39]). The process begins with an initial guess for E_{sg}, followed by numerically solving the full problem using Föppl–von Kármán equations [52] to determine the constants α_1, β_1. We then use this α_1, β_1 and Eq. (5) combined with experimental data to calculate an updated value of E_{sg}, which is further used in numerical computation to obtain a new set of α_1, β_1. We iterate this process until E_{sg} converges, ensuring the fitting logic is self-consistent. Through this process, our experiments on monolayer graphene in Fig. 2(b) suggest $E_{sg} = 1.6167$ GPa, providing a direct and quantitative measurement of the interfacial elastic coupling at the vdW gap between graphene and silicon oxide.

This methodology can be further extended for analyzing the indentation on substrate-supported n-layered graphene ($n \geqslant 2$), as shown in Fig. 3(c). Notably, in addition to the graphene/substrate interfaces, there are also $n - 1$ natural graphene/graphene interfaces (indicated by the subscript "gg"). The traction-separation relation at the graphene/graphene interface can be described by vdW interactions between two layers with finite thickness [49],

$$p_{gg}(g) = \frac{E_{gg}}{6}\left[\left(\frac{\sigma}{g(r)}\right)^5 - \left(\frac{\sigma}{g(r)}\right)^{11}\right], \quad (6)$$

where E_{gg} characterizes the interlayer elastic coupling of graphene (or the out-of-plane Young's modulus of graphite). In n-layered systems, our model suggests an indentation stiffness of

$$K_n = \left[\alpha_n + \beta_n \frac{E_{sg}}{E_{gg}} + \gamma_n\left(\frac{E_{sg}}{E_{gg}}\right)^2\right] E_{sg} r_s, \quad (7)$$

where the prefactors α_n, β_n, and γ_n are constants determined by a similar iterative process with E_{sg} as the tuning parameter. Specifically, we have $\alpha_2 = 2.4497$, $\beta_2 = -3.3242$, $\gamma_2 = 10.1742$; $\alpha_3 = 2.4548$, $\beta_3 = -6.1427$, $\gamma_3 = 21.5139$. Equation (7) extends the applicability of the model: one can easily obtain E_{sg} and E_{gg} using stiffness data from one- and two-layer experiments. Moreover, in cases where single-layer data are unavailable, interlayer modulus can still be extracted from two- and three-layer data. The numerical indentation force-displacement curves for one- to three-layered graphene from the theoretical model are shown in Fig. 4(a); they significantly depend on E_{sg}/E_{gg} (here E_{gg} is fixed; only E_{sg} is changed to tune E_{sg}/E_{gg}). However, using the indentation stiffness defined in Eqs. (5) and (7) to rescale the displacement, we find that these rescaled numerical results collapse and show a linear behavior with a slope of 1 near the zero point of the normal force. This implies that Eqs. (5) and (7) effectively capture the quantitative impact of interlayer modulus on indentation stiffness; further verifications can be found in the Supplemental Material [39]. In Fig. 3(b), we compare Eqs. (5) and (7) with the experimentally measured contact stiffnesses, allowing us to extract both E_{sg} and E_{gg}. We find the fitted $E_{gg} = (34.2 \pm 10.4$ GPa), which matches the previously reported values (33–36 GPa) [27,35] extremely well, confirming the validity of our theoretical model. The fitted elastic modulus E_{sg} for the graphene/substrate vdW interface is (1.62 ± 0.48 GPa).

V. MAPPING OF THE OUT-OF-PLANE ELASTICITY AND SCREENING EFFECT

In this section, we further investigate the impact of the 2D-3D interface on the out-of-plane mechanical properties of 2D materials. The AFM topographic image, CR-frequency mapping, and contact stiffness mapping of a monolayer and bilayer graphene on silicon substrate obtained at a small load of 42.9 nN are shown in Figs. 5(a)–5(c). Figures 5(d) and 5(e) illustrate the representative force-stiffness and the force-indentation curves of the one-layer graphene, two-layer graphene, and silicon oxide substrate. Particularly, the contact stiffnesses for one-layer, two-layer, and silicon oxide under $F_Z = 40$ nN are 160, 135, and 128 N/m, respectively. Similar to the result in Fig. 2, the out-of-plane elasticity of graphene under nonzero loading force also displays a strong layer dependence, with a rapid drop in the out-of-plane stiffness from the substrate to one layer and a less significant decrease from one layer to two layers, as shown in Figs. 5(c)–5(e).

We then conducted DFT calculations to corroborate the experimental results. We use the SIESTA code [53] to perform calculations based on density functional theory utilizing a modified van der Waals density functional [54,55], which has shown improved chemical accuracy for London dispersion forces and hydrogen bonding interactions [54]. The AFM tip is simplified to a flat plane in the DFT model and is gradually pressed down from its equilibrium position. The calculated change in force on the tip with displacement is shown in Fig. 5(f). When the tip is applied directly to the substrate, the force increases more sharply with displacement (blue curve) compared to the case in which there is graphene between the tip and the substrate (red and green curves). Moreover,

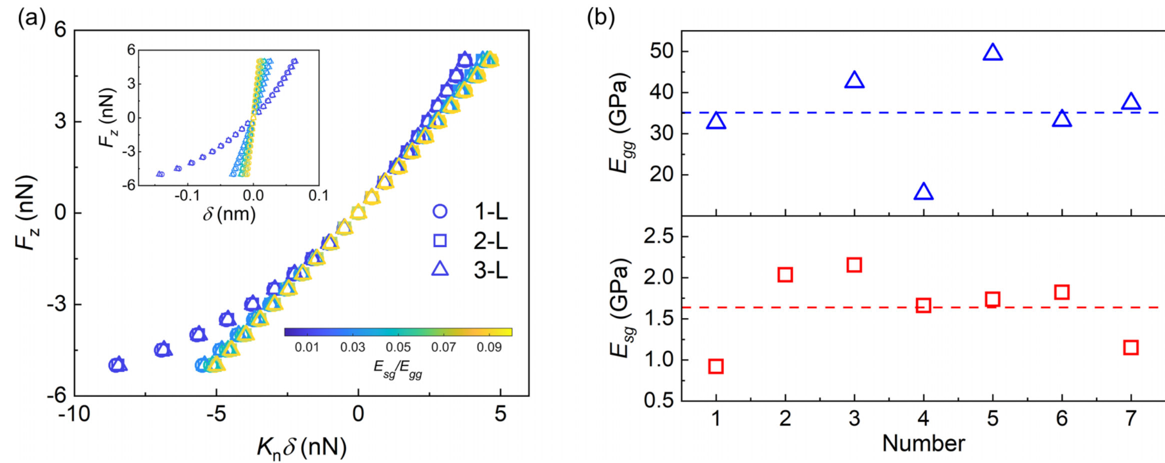

FIG. 4. (a) Rescaled force-displacement curves for one- to three-layer (distinguished by different marker shapes) graphene. Here we fix $E_{\text{gg}} = 35$ GPa and $r_s = 50$ nm, using E_{sg} as the tuning parameter for various $E_{\text{sg}}/E_{\text{gg}}$ values. The un-normalized force-displacement curves are shown in the inset. (b) The fitting results from the angstrom-indentation experiments in Fig. 2. The fitted E_{gg} and E_{sg} are (34.2 ± 11.4) GPa and (1.62 ± 0.48) GPa, respectively.

increasing the number of graphene layers reduces the force on the tip. As shown in Figs. 5(e) and 5(f), the experimental and calculated indentation curves display a similar trend, in which the rigid silicon oxide substrate seems to be "softened" in the out-of-plane direction by the supported graphene layers. This can be easily interpreted by the fact that the interfacial elastic coupling (∼1.6 GPa) is much softer than the substrate (∼75 GPa). More notably, the "softening" effect is most significant when only one 2D layer is placed on the substrate and then dramatically recedes with more 2D layers. More stiffness mapping data are presented in the Supplemental Material [39].

Previous experimental observation [56] and theoretical prediction [57] proposed a "screening effect" of 2D materials, which usually refers to the phenomenon that the existence of 2D layers between the AFM tip and substrate could significantly reduce the long-range attractive vdW interactions between the tip and substrate. In this work, we further extend the concept of "screening effect" to the repulsive regime of

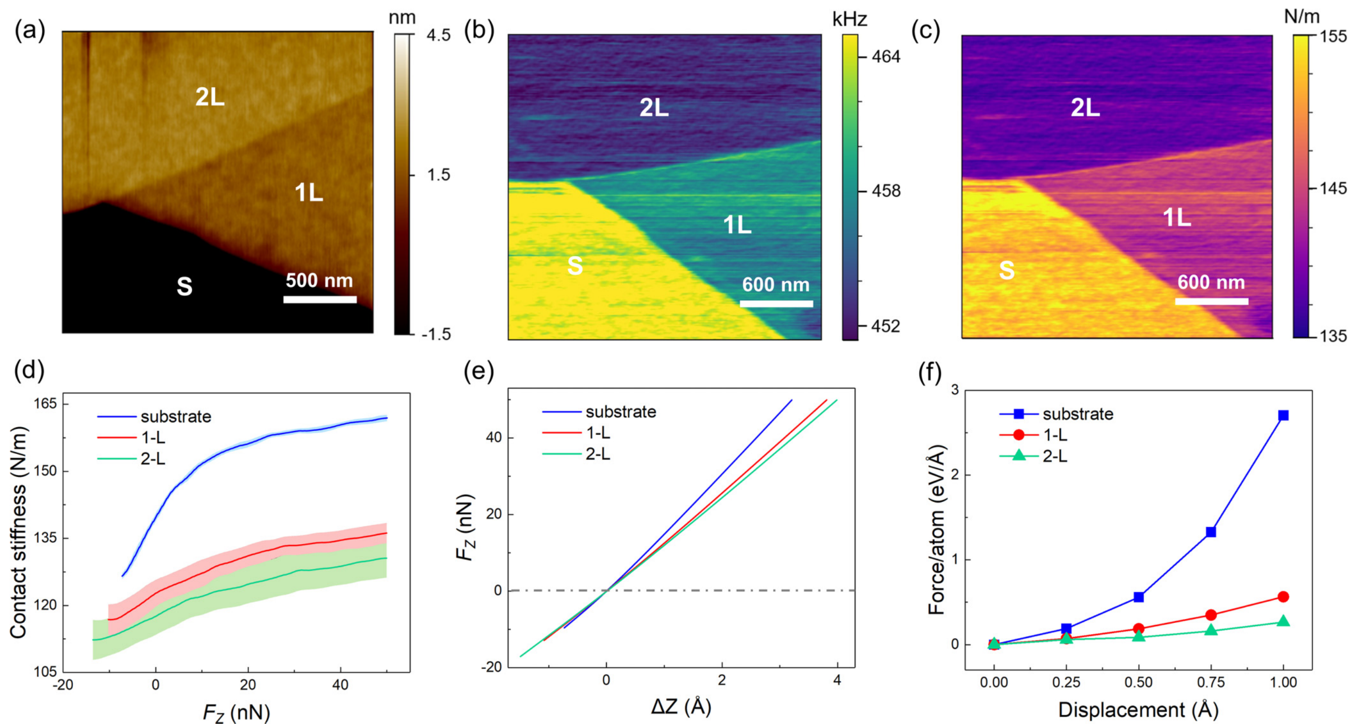

FIG. 5. (a) Topographic image, (b) contact-resonance frequency mapping, (c) contact stiffness mapping for silicon oxide substrate, and one- and two-layer graphene. (d) Contact stiffness vs loading force curves and (e) force-indentation curves for silicon oxide substrate, and one- and two-layer graphene. (f) DFT-calculated force-indentation curves for silicon oxide substrate, and one- and two-layer graphene, matching the experiments in (e).

the vdW interactions. As shown in Fig. 5, when the normal force increases to 40 nN or higher (ensuring the tip is in hard contact with the sample surface), the bare SiO_2 substrate is substantially stiffer than the case in which one or two graphene layers are placed on top. In other words, the 2D layers could significantly "screen" the repulsive vdW interaction between the AFM tip and SiO_2 substrate, and directly reduce the elastic deformation of the substrate under the normal load. A direct representation of the "screening effect" is that the SiO_2 substrate is "softened" by the 2D layers.

VI. CONCLUSIONS

In conclusion, we report the experimental measurements of the interfacial elastic coupling between few-layer graphene and the commonly used silicon oxide substrate, combined with a convenient theoretical model. It is worth noting that this method has no restrictions on the testing of 2D materials or substrates. As shown in Fig. S6 in the Supplemental Material [39], our methodology is also vaild for bilayer MoS_2 on silicon oxide. Our method could also be used to quantitatively probe the interlayer elastic coupling in the same 2D layers, as well as the elastic coupling at the vdW interface of distinct 2D layers in vdW heterostructures. For example, we demonstrate that the interlayer elastic coupling between graphene and hexagonal boron nitride is quite close to the interlayer elastic coupling in graphene via angstrom indentation, as shown in the Supplemental Material [39]. The ability to quantitatively probe the elastic coupling strength between distinct 2D layers provides the potential to modulate the interlayer vdW interactions, which directly determines the moiré potential and the exotic strongly correlated physics in 2D moiré superlattices. Moreover, the theoretical model developed here turns out to be highly successful in describing the elastic coupling between 2D materials and their supporting substrate as well as the interlayer coupling in 2D layers, greatly enriching the classical contact theory. Through local mapping of the elastic stiffness, the method reported here could effectively probe the presence of dopants or intercalates between substrate and 2D layers or within 2D layers, which are extremely important for modulating the performance of 2D electronic devices. For example, our method could be applied to test the coupling strength between 2D layers and soft substrates, which are directly related to the robustness of 2D-based flexible electronic devices. The different adhesive and deformation behaviors of soft substrates from rigid substrates may require AFM probes with softer spring constants and larger and smoother tips.

ACKNOWLEDGMENTS

X.W., Q.W., T.Z., and Y.G. acknowledge support from the Ministry of Science and Technology of China (Grant No. 2022YFA1402403) and the National Natural Science Foundation of China (Grants No. 12102386 and No. 12192211). E.C. and Z.D. acknowledge the support from the National Natural Science Foundation of China (Grants No. 12372103 and No. 12432003). X.Y. and S.Z. are supported by the National Natural Science Foundation of China (Grants No. 12272337 and No. 12002304), the Distinguished Young Scientists Fund from the Natural Science Foundation of Zhejiang Province (Grant No. LR23A020001), and the "Pioneer" R&D Program of Zhejiang (Grant No. 2023C03007).

X.W., E.C., and Q.W. contributed equally to this work. X.W. and Q.W. performed AFM experiments and data analysis. E.C. and Z.D. developed the theory. X.Y. and S.Z. performed the DFT calculations. T.Z. contributed to the AFM experiments. S.Z., Z.D. and Y.G. conceived the work. All authors contributed to discussing the data and editing the paper.

APPENDIX A: INDENTATION STIFFNESS OF BARE SUBSTRATES

Based on Eq. (4) in the main text, when the indenter approaches the bare substrate, the indentation force can be directly integrated as

$$F = \int_0^\infty 2\pi \frac{E_{\rm ss}}{6}\left[\left(\frac{\sigma}{s + r^2/2r_s}\right)^3 - \left(\frac{\sigma}{s + r^2/2r_s}\right)^9\right] r dr,$$
$$= \frac{\pi E_{\rm ss} r_s}{3}\left[\frac{\sigma^3}{2s^2} - \frac{\sigma^9}{8s^8}\right], \quad \text{(A1)}$$

where s represents the vertical separation between the bottom of the indenter and the substrate. At the zero-force point, a linear stiffness is immediately given by

$$K_0 = \frac{d}{ds}F\bigg|_{s=4^{-\frac{1}{6}}\sigma} = 2\pi E_{\rm ss} r_s. \quad \text{(A2)}$$

APPENDIX B: INDENTATION STIFFNESS OF GRAPHENE-COVERED SUBSTRATES

The presence of graphene layers between the indenter and the substrate introduces possible nonlinear deformations. For example, for the indentation of a single-layer graphene, the vertical displacement w satisfies the out-of-plane equilibrium equation,

$$B\nabla_r\nabla_r w - \frac{1}{r}\frac{d}{dr}\left(\frac{d\varphi}{dr}\frac{dw}{dr}\right) + p_{\rm sg}(w+\sigma)$$
$$- p_{\rm sg}[q(r) - w] = 0, \quad \text{(B1)}$$

and strain compatibility equation,

$$r\frac{d}{dr}\left[\frac{1}{r}\frac{d}{dr}\left(r\frac{d\varphi}{dr}\right)\right] = -\frac{1}{2}Et\left(\frac{dw}{dr}\right)^2, \quad \text{(B2)}$$

where $\nabla_r f = \frac{d^2 f}{dr^2} + \frac{1}{r}\frac{df}{dr}$ and φ is the Airy stress function. Note that we have modeled the indenter shape as a parabola so $q(r) = s + r^2/2r_s$. We solve this problem numerically in the Supplemental Material [39]. Despite the complex nonlinearities in this indentation problem, we show that Eqs. (5) and (7) can be utilized to analyze the experimental measurements with iterative fitting.

[1] K. S. Novoselov, A. K. Geim, S. V. Morozov, D. Jiang, Y. Zhang, S. V. Dubonos, I. V. Grigorieva, and A. A. Firsov, Electric field effect in atomically thin carbon films, Science 306, 666 (2004).

[2] K. S. Novoselov, A. Mishchenko, A. Carvalho, and A. H. Castro Neto, 2D materials and van der Waals heterostructures, Science **353**, aac9439 (2016).

[3] J. R. Schaibley, H. Yu, G. Clark, P. Rivera, J. S. Ross, K. L. Seyler, W. Yao, and X. Xu, Valleytronics in 2D materials, Nat. Rev. Mater. **1**, 16055 (2016).

[4] D. Akinwande, C. J. Brennan, J. S. Bunch, P. Egberts, J. R. Felts, H. Gao, R. Huang, J.-S. Kim, T. Li, Y. Li *et al.*, A review on mechanics and mechanical properties of 2D materials—Graphene and beyond, Extreme Mech. Lett. **13**, 42 (2017).

[5] L. Liu, T. Li, L. Ma, W. Li, S. Gao, W. Sun, R. Dong, X. Zou, D. Fan, L. Shao *et al.*, Uniform nucleation and epitaxy of bilayer molybdenum disulfide on sapphire, Nature (London) **605**, 69 (2022).

[6] J. Zhao, P. Ji, Y. Li, R. Li, K. Zhang, H. Tian, K. Yu, B. Bian, L. Hao, X. Xiao *et al.*, Ultrahigh-mobility semiconducting epitaxial graphene on silicon carbide, Nature (London) **625**, 60 (2024).

[7] F. Wu, H. Tian, Y. Shen, Z. Hou, J. Ren, G. Gou, Y. Sun,Y. Yang, and T.-L. Ren, Vertical MoS_2 transistors with sub-1-nm gate lengths, Nature (London) **603**, 259 (2022).

[8] S. J. Kim, K. Choi, B. Lee, Y. Kim, and B. H. Hong, Materials for flexible, stretchable electronics: Graphene and 2D materials, Annu. Rev. Mater. Res. **45**, 63 (2015).

[9] Z. Dai, N. Lu, K. M. Liechti, and R. Huang, Mechanics at the interfaces of 2D materials: Challenges and opportunities, Curr. Opin. Solid State Mater. Sci. **24**, 100837 (2020).

[10] B. Li, J. Yin, X. Liu, H. Wu, J. Li, X. Li, and W. Guo, Probing van der Waals interactions at two-dimensional heterointerfaces, Nat. Nanotechnol. **14**, 567 (2019).

[11] X. Liu and M. C. Hersam, Interface characterization and control of 2D materials and heterostructures, Adv. Mater. **30**, e1801586 (2018).

[12] S. Lippert, L. M. Shneider, D. Renaud, K. N. Kang, O. Ajayi, J. Kuhnert, M. U. Halbich, O. M. Abdulmunem, X. Lin, K. Hassoon *et al.*, Influence of the substrate material on the optical properties of tungsten diselenide monolayers, 2D Mater. **4**, 025045 (2017).

[13] R. Dong, T. Zhang, and X. Feng, Interface-assisted synthesis of 2D materials: Trend and challenges, Chem. Rev. **118**, 6189 (2018).

[14] X. Zhang, Y. Zhang, H. Yu, H. Zhao, Z. Cao, Z. Zhang, and Y. Zhang, Van der Waals-interface-dominated all-2D electronics, Adv. Mater. **35**, 2207966 (2023).

[15] D. S. Schulman, A. J. Arnold, and S. Das, Contact engineering for 2D materials and devices, Chem. Soc. Rev. **47**, 3037 (2018).

[16] J. Cheng, C. Wang, X. Zou, and L. Liao, Recent advances in optoelectronic devices based on 2D materials and their heterostructures, Adv. Opt. Mater. **7**, 1800441 (2019).

[17] A. K. Geim and I. V. Grigorieva, Van der Waals heterostructures, Nature (London) **499**, 419 (2013).

[18] Y. Liu, N. O. Weiss, X. Duan, H.-C. Cheng, Y. Huang, and X. Duan, Van der Waals heterostructures and devices, Nat. Rev. Mater. **1**, 16042 (2016).

[19] Y. Cao, V. Fatemi, A. Demir, S. Fang, S. L. Tomarken, J. Y. Luo, J. D. Sanchez-Yamagishi, K. Watanabe, T. Taniguchi, E. Kaxiras *et al.*, Correlated insulator behaviour at half-filling in magic-angle graphene superlattices, Nature **556**, 80 (2018).

[20] Y. Cao, V. Fatemi, S. Fang, K. Watanabe, T. Taniguchi, E. Kaxiras, and P. Jarillo-Herrero, Unconventional superconductivity in magic-angle graphene superlattices, Nature (London) **556**, 43 (2018).

[21] C. Jin, E. C. Regan, A. Yan, M. Iqbal Bakti Utama, D. Wang, S. Zhao, Y. Qin, S. Yang, Z. Zheng, S. Shi *et al.*, Observation of moire excitons in WSe_2/WS_2 heterostructure superlattices, Nature (London) **567**, 76 (2019).

[22] Y. Tang, L. Li, T. Li, Y. Xu, S. Liu, K. Barmak, K. Watanabe, T. Taniguchi, A. H. MacDonald, J. Shan *et al.*, Simulation of Hubbard model physics in WSe_2/WS_2 moire superlattices, Nature (London) **579**, 353 (2020).

[23] K. Tran, G. Moody, F. Wu, X. Lu, J. Choi, K. Kim, A. Rai, D. A. Sanchez, J. Quan, A. Singh *et al.*, Evidence for moire excitons in van der Waals heterostructures, Nature (London) **567**, 71 (2019).

[24] E. Han, J. Yu, E. Annevelink, J. Son, D. A. Kang, K. Watanabe, T. Taniguchi, E. Ertekin, P. Y. Huang, and A. M. van der Zande, Ultrasoft slip-mediated bending in few-layer graphene, Nat. Mater. **19**, 305 (2020).

[25] M. Rejhon, F. Lavini, A. Khosravi, M. Shestopalov, J. Kunc, E. Tosatti, and E. Riedo, Relation between interfacial shear and friction force in 2D materials, Nat. Nanotechnol. **17**, 1280 (2022).

[26] C. Lee, X. Wei, J. W. Kysar, and J. Hone, Measurement of the elastic properties and intrinsic strength of monolayer graphene, Science **321**, 385 (2008).

[27] Y. Gao, S. Kim, S. Zhou, H.-C. Chiu, D. Nélias, C. Berger, W. de Heer, L. Polloni, R. Sordan, A. Bongiorno *et al.*, Elastic coupling between layers in two-dimensional materials, Nat. Mater. **14**, 714 (2015).

[28] K. Liu and J. Wu, Mechanical properties of two-dimensional materials and heterostructures, J. Mater. Res. **31**, 832 (2015).

[29] A. Castellanos-Gomez, M. Poot, G. A. Steele, H. S. J. van der Zant, N. Agraït, and G. Rubio-Bollinger, Elastic properties of freely suspended MoS_2 nanosheets, Adv. Mater. **24**, 772 (2012).

[30] S. Bertolazzi, J. Brivio, and A. Kis, Stretching and breaking of ultrathin MoS_2, ACS Nano **5**, 9703 (2011).

[31] F. Cellini, Y. Gao, and E. Riedo, Å-Indentation for non-destructive elastic moduli measurements of supported ultra-hard ultra-thin films and nanostructures, Sci. Rep. **9**, 4075 (2019).

[32] Y. Gao, T. Cao, F. Cellini, C. Berger, W. A. de Heer, E. Tosatti, E. Riedo, and A. Bongiorno, Ultrahard carbon film from epitaxial two-layer graphene, Nat. Nanotechnol. **13**, 133 (2018).

[33] M. Rejhon, V. Dědič, V. M. Shestopalov, J. Kunc, and E. Riedo, Impact of metastable graphene-diamond coatings on the fracture toughness of silicon carbide, Nanoscale **16**, 10590 (2024).

[34] M. Rejhon, X. Zhou, F. Lavini, A. Zanut, F. Popovich, L. Schellack, L. Witek, P. Coelho Giant, J. Kunc, and E. Riedo, Increase of hardness in silicon carbide by metastable single layer diamond-like coating, Adv. Sci. **10**, e2204562 (2023).

[35] B. T. Kelly, *Physics of Graphite* (Applied Science, London, 1981).

[36] Z.-Y. Zheng, Y.-H. Pan, T.-F. Pei, R. Xu, K.-Q. Xu, L. Lei, S. Hussain, X.-J. Liu, L.-H. Bao, H.-J. Gao *et al.*, Local probe of the interlayer coupling strength of few-layers SnSe by contact-resonance atomic force microscopy, Front. Phys. **15**, 63505 (2020).

[37] Q. Tu, B. Lange, Z. Parlak, J. M. J. Lopes, V. Blum, and S. Zauscher, Quantitative subsurface atomic structure fingerprint for 2D materials and heterostructures by

first-principles-calibrated contact-resonance atomic force microscopy, ACS Nano **10**, 6491 (2016).

[38] Z. Abooalizadeh, P. Gong, L. Sudak, and P. Egberts, Layer dependent out-of-plane elastic modulus of graphene, Appl. Phys. Lett. **118**, 263101 (2021).

[39] See Supplemental Material at http://link.aps.org/supplemental/10.1103/PhysRevB.111.125418 for the detailed experimental setup and background theory for the angstrom-indentation method; the raw experimental data; detailed verification and discussion of the contact theory developed in this paper; angstrom-indentation data for graphene/h-BN heterostructure and bilayer; settings of the DFT calculations, which also contains Refs. [40–48].

[40] Y. Wang, C. Wu, J. Tang, M. Duan, J. Chen, B.-F. Ju, and Y.-L. Chen, Measurement of sub-surface microstructures based on a developed ultrasonic atomic force microscopy, Appl. Sci. **12**, 5460 (2022).

[41] U. Rabe, S. Amelio, E. Kester, V. Scherer, S. Hirsekorn, and W. Arnold, Quantitative determination of contact stiffness using atomic force acoustic microscopy, Ultrasonics **38**, 430 (2000).

[42] F. J. Espinoza-Beltrán, K. Geng, J. Muñoz Saldaña, U. Rabe, S. Hirsekorn, and W. Arnold, Simulation of vibrational resonances of stiff AFM cantilevers by finite element methods, New J. Phys. **11**, 083034 (2009).

[43] J. L. Feldman, Elastic constants of $2H$-MoS_2 and $2H$-$NbSe_2$ extracted from measured dispersion curves and linear compressibilities, J. Phys. Chem. Solids **37**, 1141 (1976).

[44] H. Peelaers and C. G. Van de Walle, Elastic constants and pressure-induced effects in MoS_2, J. Phys. Chem. C **118**, 12073 (2014).

[45] Y. Kopelevich and P. Esquinazi, Graphene physics in graphite, Adv. Mater. **19**, 4559 (2007).

[46] X.-Y. Ren, C.-X. Zhao, C.-Y. Niu, J.-Q. Wang, Y. Jia, and J.-H. Cho, First-principles study of the crystal structures and physical properties of H18-BN and Rh6-BN, Phys. Lett. A **380**, 3891 (2016).

[47] M. Grimsditch, E. S. Zouboulis, and A. Polian, Elastic constants of boron nitride, J. Appl. Phys. **76**, 832 (1994).

[48] A. K. Geim, Graphene: Status and prospects, Science **324**, 1530 (2009).

[49] J. N. Israelachvili, *Intermolecular and Surface Forces* (Academic Press, New York, 2011).

[50] J. R. Barber, *Contact Mechanics* (Springer, Berlin, 2018).

[51] B. V. Derjaguin, V. M. Muller, and Y. P. Toporov, Effect of contact deformations on the adhesion of particles, J. Colloid Interface Sci. **53**, 314 (1975).

[52] E. H. Mansfield, *The Bending and Stretching of Plates* (Cambridge University Press, Cambridge, 1989).

[53] M. S. José, J. D. Gale Artacho, A. García, J. Junquera, P. Ordejón, and D. Sánchez-Portal, The SIESTA method for *ab initio* order-N materials simulation, J.Phys.: Condens. Matter **14**, 2745 (2002).

[54] J. Klimeš, D. R. Bowler, and A. Michaelides, Chemical accuracy for the van der Waals density functional, J. Phys.: Condens. Matter **22**, 022201 (2010).

[55] M. Dion, H. Rydberg, E. Schröder, D. C. Langreth, and B. I. Lundqvist, van der Waals density functional for general geometries, Phys. Rev. Lett. **92**, 246401 (2004).

[56] S. Tsoi, P. Dev, A. L. Friedman, R. Stine, J. T. Robinson, T. L. Reinecke, and P. E. Sheehan, van der Waals screening by single-layer graphene and molybdenum disulfide, ACS Nano **8**, 12410 (2014).

[57] X. Liu, Z. Zhang, and W. Guo, van der Waals screening by graphenelike monolayers, Phys. Rev. B **97**, 241411(R) (2018).